HHS Public Access

Author manuscript

Neuroimage. Author manuscript; available in PMC 2023 August 30.

Published in final edited form as:

Neuroimage. 2021 July 15; 235: 118012. doi:10.1016/j.neuroimage.2021.118012.

In vivo evaluation of heme and non-heme iron content and neuronal density in human basal ganglia ☆

Dmitriy A Yablonskiy[a,*], **Jie Wen**[b], **Satya V.V.N. Kothapalli**[a], **Alexander L Sukstanskii**[a]

[a]Department of Radiology, Washington University in St. Louis, 4525 Scott Ave. Room 3216, St. Louis, MO 63110, United States

[b]Department of Radiology, The First Affiliated Hospital of USTC, Hefei, Anhui 230001, China

Abstract

Non-heme iron is an important element supporting the structure and functioning of biological tissues. Imbalance in non-heme iron can lead to different neurological disorders. Several MRI approaches have been developed for iron quantification relying either on the relaxation properties of MRI signal or measuring tissue magnetic susceptibility. Specific quantification of the non-heme iron can, however, be constrained by the presence of the heme iron in the deoxygenated blood and contribution of cellular composition. The goal of this paper is to introduce theoretical background and experimental MRI method allowing disentangling contributions of heme and non-heme irons simultaneously with evaluation of tissue neuronal density in the iron-rich basal ganglia. Our approach is based on the quantitative Gradient Recalled Echo (qGRE) MRI technique that allows separation of the total $R2^*$ metric characterizing decay of GRE signal into tissue-specific ($R2t^*$) and the baseline blood oxygen level-dependent (BOLD) contributions. A combination with the QSM data (also available from the qGRE signal phase) allowed further separation of the tissue-specific $R2t^*$ metric in a cell-specific and non-heme-iron-specific contributions. It is shown that the non-heme iron contribution to $R2t^*$ relaxation can be described with the previously developed Gaussian Phase Approximation (GPA) approach. qGRE data were obtained from 22 healthy control participants (ages 26–63 years). Results suggest that the ferritin complexes are aggregated in clusters with an average radius about 100 nm comprising approximately 2600 individual ferritin units. It is also demonstrated that the concentrations of heme and non-heme iron tend to increase

☆Preliminary results of this study were presented at ISMRM-2019 annual meeting

*Corresponding author. yablonskiyd@wustl.edu (D.A. Yablonskiy).

Data and code availability statements

Data were obtained from 22 healthy control participants (ages 26–63 years) with the local IRB approval from Washington University in Saint Louis. The written informed consent was obtained from all participants.

Data are available via a request to the Authors, through a formal data sharing agreement.

Algorithms for generating the qGRE metrics from raw data were published previously and are clearly cited in the submitted manuscript.

QSM maps were generated using publicly available software: http://weill.cornell.edu/mri/pages/qsm.html

Credit authorship contribution statement

Dmitriy A Yablonskiy: Conceptualization, Methodology, Formal analysis, Writing – original draft, Writing – review & editing, Visualization, Supervision, Project administration, Funding acquisition. **Jie Wen:** Software, Validation, Formal analysis, Investigation, Data curtion, Visualization, Writing – review & editing. **Satya V.V.N. Kothapalli:** Software, Formal analysis, Data curation, Visualization, Writing – review & editing. **Alexander L Sukstanskii:** Methodology, Formal analysis, Visualization, Writing – original draft, Writing – review & editing.

with age. The strongest age effect was seen in the pallidum region, where the highest age-related non-heme iron accumulation was observed.

Keywords

Quantitative gradient recalled echo MRI; QSM; Brain iron; $R2^*$; $R2t^*$; BOLD; Neuronal density

1. Introduction

Iron is an important element supporting the structure and functioning of biological tissues. In the brain, heme iron in the hemoglobin supports oxygen delivery while most of the brain non-heme ferric iron is believed to be present as a storage pool consisting of ferritin or hemosiderin (Schenck 1992; Schenck and Zimmerman 2004). Imbalance in non-heme iron in the brain can lead to different neurological disorders (Schenck 1992; Stankiewicz et al., 2007). Of all chemical elements present in the brain, iron has the biggest magnetic moment (closely followed only by oxygen O_2) thus affecting MRI signal relaxation properties ($T1$, $T2$, $T2^*$) which is the basis of several MRI approaches for iron quantification (e.g. (Schenck and Zimmerman 2004; Stankiewicz et al., 2007; Peran et al., 2009; Yao et al., 2009; Langkammer et al., 2010; Langkammer et al., 2012; Li et al., 2014; Sedlacik et al., 2014; Barbosa et al., 2015; Liu et al., 2016; Taege et al., 2019)).

Quantitative Susceptibility Mapping (QSM) technique (see latest reviews (Reichenbach et al., 2015; Wang and Liu 2015)) allows evaluation of tissue magnetic susceptibility based on the MRI signal phase. Due to the paramagnetic nature, iron significantly contributes to the tissue magnetic susceptibility and can be detected by QSM (Langkammer et al., 2012). However, the in vivo quantification of the non-heme iron can be constrained by the heme iron in the deoxygenated blood and contribution of other cell-building materials (proteins, lipids, etc.). On the other hand, a quantitative Gradient Recalled Echo (qGRE) MRI (Ulrich and Yablonskiy 2016) provides a quantitative information on the baseline brain tissue concentration of deoxyhemoglobin and the tissue-related GRE signal decay rate $R2t^*$ from which information on the brain cellular composition can be inferred (Wen et al., 2018). The goal of this paper is to introduce an experimental method that combines QSM and qGRE MRI to allow disentangling contributions of heme and non-heme irons and tissue cellular structure in the basal ganglia.

2. Theory

2.1. qGRE provides information on Gray Matter heme iron and tissue cellular composition

qGRE technique (Ulrich and Yablonskiy 2016) is based on 3D GRE MRI sequence with multiple gradient echoes, our theoretical model of BOLD (Yablonskiy and Haacke 1994; Yablonskiy 1998) and cellular (Ulrich and Yablonskiy 2016; Wen et al., 2018) contributions to the GRE signal decay, and algorithms that we have developed for correcting adverse effects of background field gradients (Yablonskiy et al., 2013) and physiological fluctuations (Wen et al., 2015). In the framework of this approach, the GRE signal dependence on the

echo time TE is presented in the following form (Yablonskiy 1998; Ulrich and Yablonskiy 2016)

$$S(TE) = S_0 \cdot \exp(-R2t^* \cdot TE) \cdot F_{BOLD}(TE) \cdot F_{macro}(TE) \cdot \exp(i \cdot 2\pi \cdot \Delta f \cdot TE) \quad (1)$$

where S_0 is the signal amplitude, the $R2t^*$ is the tissue-specific relaxation rate constant (here "t" means $tissue$), the factor $F_{BOLD}(TE)$ describes contribution of the baseline Blood Oxygen Level Dependent (BOLD) (Yablonskiy and Haacke 1994; Yablonskiy 1998) effects to the signal decay, the function $F_{macro}(TE)$ describes the effects of macroscopic magnetic field inhomogeneities (herein we use the Voxel Spread Function (VSF) method (Yablonskiy et al., 2013) to calculate $F_{macro}(TE)$), and Δf is the frequency shift (dependent on tissue structure as well as on macroscopic magnetic field inhomogeneities created mostly by tissue/air interfaces). Such a factorization of different contributions to the GRE signal is possible due to the difference in their spatial scales (Yablonskiy 1998) – *microscopic* (cellular level), *mesoscopic* (distances that are much larger than the cellular scale but smaller than the imaging voxel size), and *macroscopic* (distances larger than the imaging voxel size). At the microscopic level, cellular and subcellular interactions are responsible for the cell-specific part of the $R2t^*$ relaxation. Blood vessels are positioned at the mesoscopic level as an average distance between capillaries is about 50 μm, while a typical voxel size in MRI experiments is about 1 mm. Finally, adverse background B_0 field gradients have a scale larger than the voxel size as they originate from the sources (mostly tissue/air interfaces) that are usually outside of the voxel.

Note that Eq. (1) suggests that the tissue-related relaxation factor in GM can be described by a single relaxation rate constant $R2t^*$. The latter has contributions from cellular components - $R2t^*_{cell}$ (Zhao et al., 2016; Wen et al., 2018), and non-heme iron - $R2t^*_{nhi}$:

$$R2t^* = R2t^*_{cell} + R2t^*_{nhi} \quad (2)$$

Using a concept of cells as endogenous contrast agent, it was demonstrated in (Wen et al., 2018), that in the GM of healthy adult human brains at 3T MRI the cellular term, $R2t^*_{cell}$, is related to the neuronal density index NDI (parameter proportional to the neuronal density):

$$R2t^*_{cell} = 5.8 + 20.4 \cdot NDI \quad (3)$$

where $R2t^*_{cell}$ is measured in s^{-1} and NDI is dimensionless parameter ranging between 0 (tissue void of neurons but containing other cells and cellular components) and 1 (tissue comprised of neuronal cells only). The quantitative relationship in Eq. (3) established in (Wen et al., 2018) was based on the analysis of the gene expression profiles across the healthy adult human brain GM obtained from the Allan Human Brain Atlas and a profile of the $R2t^*_{cell}$ metric of qGRE signal. It was demonstrated that the expression profiles of genes that are mainly associated with neuronal processes (axons and dendrites) were strongly correlated with $R2t^*_{cell}$, thus suggesting that neurons are the *strongest endogenous contrast*

agent contributing to $R2t^*_{cell}$. Hence, $R2t^*_{cell}$-derived NDI can be used as a proxy that largely represents neuronal contribution to the brain tissue cellular composition.

The heme-iron-related BOLD factor, $F_{BOLD}(TE)$, is as follows (Yablonskiy and Haacke 1994):

$$F_{BOLD}(TE) = \exp\left[-dCBV \cdot f_c(\delta\omega_h \cdot TE)\right] \tag{4}$$

where $dCBV$ is the deoxygenated cerebral blood volume fraction (deoxyhemoglobin-containing part of the total blood volume, i.e. veins and adjacent to them portion of the capillary bed). The function f_c can be expressed in terms of a generalized hypergeometric function ${}_1F_2$ (Yablonskiy et al., 2013a):

$$f_c(\omega_h \cdot TE) = {}_1F_2\left(\left[-\frac{1}{2}\right];\left[\frac{3}{4},\frac{5}{4}\right];\ -\frac{9}{16}(\delta\omega_h \cdot TE)^2\right) - 1 \tag{5}$$

The important feature of function f_c is a quadratic (with respect to TE) behavior for short $TE < t_*$, $t_* = 1.5\ /\ \delta\omega_h$ and linear behavior in the opposite case $TE > t_*$. In the latter case, the BOLD factor in Eq. (1) reduces to a mono-exponential function and can be described by means of the relaxation rate parameter $R2'_{BOLD}$:

$$\begin{aligned} &F_{BOLD}(TE) = \exp\left(-R2'_{BOLD} \cdot TE\right), \\ &R2'_{BOLD} = dCBV \cdot \delta\omega_h, \qquad TE > t_* \end{aligned} \tag{6}$$

The characteristic frequency $\delta\omega_h$ is determined by the external magnetic field B_0 and the magnetic susceptibility $\Delta\chi^{(0)}_{heme}$, which is the difference between volume magnetic susceptibilities of deoxygenated blood and the surrounding brain tissue (Yablonskiy and Haacke 1994):

$$\delta\omega_h = \frac{1}{3} \cdot \gamma \cdot B_0 \cdot \Delta\chi^{(0)}_{heme} \tag{7}$$

where $\gamma = 2.675 \cdot 10^8\ \mathrm{rad \cdot s^{-1} \cdot T^{-1}}$ is the gyromagnetic ratio. Note that SI units are used herein. The magnetic susceptibility $\Delta\chi^{(0)}_{heme}$ is due to the presence of heme iron in red blood cells and depends on the blood oxygenation level Y ($Y = 0$ corresponds to fully deoxygenated, and $Y = 1$ to fully oxygenated blood) and blood hematocrit Hct (Yablonskiy and Haacke 1994):

$$\Delta\chi^{(0)}_{heme} = \Delta\chi_0 \cdot Hct \cdot (1 - Y) \tag{8}$$

Here $\Delta\chi_0 = 4\pi \cdot 0.27\ ppm$ (Spees et al., 2001) is the susceptibility difference between fully oxygenated and fully deoxygenated red blood cells.

The magnetic susceptibility of heme iron per unit tissue volume (volume magnetic susceptibility) can then be calculated as:

$$\Delta\chi_{heme} = \Delta\chi^{(0)}_{heme} \cdot dCBV \tag{9}$$

Hence, $\Delta\chi_{heme}$ can be found from the qGRE-defined BOLD-related parameter $R2'_{BOLD}$, Eq. (6) and Eqs. (7-9):

$$\Delta\chi_{heme} = \Delta\chi_0 \cdot Hct \cdot (1-Y) \cdot dCBV = \frac{3 \cdot R2'_{BOLD}}{\gamma B_0} \tag{10}$$

2.2. QSM provides information on the spatial variation of the total tissue magnetic susceptibility in Gray Matter

From the QSM experiment, a spatial variation in the local magnetic susceptibility of Gray Matter (GM), $\Delta\chi_{QSM}$, can be obtained (Reichenbach et al., 2015; Wang and Liu 2015). Thus, combining qGRE with QSM, we can find contribution of the magnetic susceptibility of *non-heme iron* $\Delta\chi_{nhi}$ to the total tissue magnetic susceptibility:

$$\Delta\chi_{nhi} = \Delta\chi_{QSM} - \Delta\chi_{heme} - \Delta\chi_{cell} \tag{11}$$

where $\Delta\chi_{cell}$ is a cellular contribution to $\Delta\chi_{QSM}$ that excludes contribution of heme and non-heme iron. Importantly, in this equation, $\Delta\chi_{nhi}$ and $\Delta\chi_{heme}$ are magnetic susceptibility differences between non-heme / heme iron and surrounding cellular environment. Such a separation is possible because concentrations of blood vessels (the source of heme iron) and of non-heme iron clusters are very small; hence their contributions to the total tissue magnetic susceptibility are independent. As magnetic susceptibility of iron (which is paramagnetic) is significantly higher (about three orders of magnitude) than the magnetic susceptibility of cell-building molecules (proteins, lipids, etc., that are diamagnetic), in the areas of high iron accumulation (e.g., basal ganglia, which are of interest for us), the term $\Delta\chi_{cell}$ gives only small contribution to $\Delta\chi_{QSM}$. In this paper we will account for cellular contribution by referencing QSM measurements in basal ganglia to QSM measurements in cortical GM where concentration of iron is significantly lower than in the basal ganglia (Hallgren and Sourander 1958a). This issue will be further addressed in the Methods section.

2.3. Contribution of non-heme iron to GRE signal relaxation

Non-heme ferric iron (Fe^{3+}) in the brain is stored mostly in ferritin. The iron-free apoferritin protein is an approximately hollow spherical shell with an inner radius $R_{in} = 4$ nm and external radius $R_{ext} = 6.25$ nm (Cornell and Schwertmann 2003). Excess tissue iron is deposited within the hollow cavity of this protein as a mineralized iron oxide particle attached to the inner wall of the sphere, containing up to $N_i = 4500$ iron atoms as superparamagnetic crystalline ferric oxyhydroxide, known as ferrihydrite ($5Fe_2O_3 \cdot 9H_2O$).

Measurements of magnetization M versus field H performed on ferritin in solution at 3 °C and 23 °C (Michaelis et al., 1943; Quintana et al., 2004) revealed that this dependence can be well described by the Curie law, albeit with an atypical (for Fe^{3+}) moment $\mu_{eff} = 3.8\,\mu_B$ (μ_B is the Bohr magneton). The latter property was attributed to an unusual electronic

configuration of ferrihydrite. Hence, the paramagnetic contribution of the Fe^{3+} molecules to the magnetic susceptibility of the ferritin core can be calculated using Curie's Law:

$$\chi_{ferr\ core}^{(par)} = n \cdot \frac{\mu_0 \cdot \mu_{eff}^2}{3k_B T} \tag{12}$$

where μ_0 is the permeability of free space, $n = N_i / (4\pi \cdot R_{\text{int}}^3 / 3)$ is the concentration of iron atoms within the ferritin core, k_B is the Boltzmann constant, and T is temperature. Accordingly, for $N_i = 4500$ at $T = 310^{\circ}\text{K}$ we get in SI units

$$\chi_{ferr\ core}^{(par)} = 2018\,\text{ppm} \tag{13}$$

Another important characteristic is an average magnetic susceptibility of ferritin that can be calculated using the above theoretical equations but with R_{ext} instead of R_{int}. The result is:

$$\chi_{ferr} = 529\,\text{ppm} \tag{14}$$

as first reported by Schenck (Schenck 1992). Note that the actual value of magnetic susceptibility of the whole iron-laden ferritin complex is slightly different from that in Eq. (14) due to the presence of the diamagnetic protein shell in the ferritin complex. However, since the magnetic susceptibility of proteins is only about few ppm, this contribution is less than 1% of the paramagnetic contribution of the iron core (2018 ppm) and accounting for it would be beyond the accuracy of the above-made assumptions based on the existing information on ferritin structure.

When calculating the non-heme iron contribution to the GRE signal decay, the ferritin particles can be considered as spherical susceptibility inclusions with the magnetic susceptibility per Eq. (14) and radius R_{ext}. An analysis of such a problem should take into account an inhomogeneous magnetic field induced by the susceptibility inclusions (leading to signal dephasing) as well as diffusion of water molecules in this field. Generally, an exact solution to the problem is unavailable, therefore, in what follows, we will consider it in two opposite limiting cases: (i) in the static dephasing regime (SDR) when diffusion plays negligible role (Yablonskiy and Haacke 1994), and (ii) in the motional narrowing regime (MNR) when diffusion significantly reduces the signal decay rate (herein we will use the Gaussian Phase Approximation (GPA) (Sukstanskii and Yablonskiy 2003; Sukstanskii and Yablonskiy 2004) to describe signal in the MNR).

In the framework of the SDR, the signal decay induced by the randomly distributed ferritin spheres can be presented as in Eq. (4) with the substitutions $dCBV \rightarrow \zeta_{ferr}$ and $f_c(\delta\omega_h \cdot TE) \rightarrow f_s(\delta\omega_f \cdot TE)$ (Yablonskiy and Haacke 1994), where ζ_{ferr} is the non-heme iron (ferritin) volume fraction, and the characteristic frequency $\delta\omega_f$ is

$$\delta\omega_f = \frac{1}{3} \cdot \gamma \cdot B_0 \cdot (\chi_{ferr} - \chi_{tissue}) \tag{15}$$

Given that $\chi_{tissue} \approx \chi_{water} = -9$ ppm, we find for $B_0 = 3$T, $\delta\omega_f = 0.14 \cdot 10^6\,\mathrm{s}^{-1}$. Since the transition time $t_* = 1.5 / \delta\omega_f$ separating the quadratic and linear regimes in function f_s (Yablonskiy and Haacke 1994) is very short ($t_* = 10$ μs), the quadratic regime cannot be captured in our experiment (see details below) with minimum TE of 4 ms . Thus, the contribution of non-heme iron to the GRE signal decay can be described by a simple exponential function

$$F_{nhi}(TE) = \exp(-R2t^*_{nhi} \cdot TE);$$
$$R2t^*_{nhi} = \lambda_{SDR} \cdot \Delta\chi_{nhi}, \quad \lambda_{SDR} = \frac{2\pi}{9\sqrt{3}} \cdot \gamma \cdot B_0 \tag{16}$$

where $\Delta\chi_{nhi}$ is the volume magnetic susceptibility of non-heme iron with respect to the iron-free tissue:

$$\Delta\chi_{nhi} = (\chi_{ferr} - \chi_{tissue}) \cdot \zeta_{ferr} \tag{17}$$

It should be emphasized, however, that the SDR, in which diffusion of water molecules does not affect signal decay, is valid only when the radius of spherical susceptibility inclusions is large enough (Yablonskiy and Haacke 1994):

$$R > \widetilde{R} = \left(\frac{2D}{\delta\omega_f \cdot \zeta_{ferr}^{1/3}}\right)^{1/2} \tag{18}$$

where $D \sim 1$ μm^2/ms is the diffusion coefficient of water molecules in the brain tissue. The ferritin volume fraction can be readily related to the non-heme iron concentration $[Fe]$:

$$\zeta_{ferr} = \frac{\rho_t \cdot N_a}{M_{Fe} \cdot n} \cdot \left(\frac{R_{ext}}{R_{\mathrm{int}}}\right)^3 \cdot [Fe] \tag{19}$$

where $[Fe]$ is measured in μg Fe per gram of wet tissue, $M_{Fe} = 56$ g/mol is the atomic weight of iron and $\rho_t = 1.05$ g/cm^3 is the brain tissue density (Barber et al., 1970); iron molecular density (n) is the same as in Eq. (12), and N_a is the Avogadro number. For iron-rich ROIs of interest, iron concentration is about 200 μg/g (Hallgren and Sourander 1958b; Krebs et al., 2014), that corresponding to $\zeta_{ferr} \sim 2 \cdot 10^{-4}$. Thus, to satisfy the criterion in Eq. (18) for $B_0 = 3$T, the radius of susceptibility inclusions must be bigger than $\widetilde{R} \approx 0.4$ μm which greatly exceeds the radius of a single ferritin complex $R_{ext} = 6.25$ nm. Consequently, at $B_0 = 3$T MRI, the SDR can be applied to ferritin in the brain only if the ferritin complexes are aggregated in clusters with the size about 0.4 μm or more. Note, that the criterion in Eq. (18) scales as $B_0^{-1/2}$ and for 7T would be valid for clusters of smaller sizes, about 0.26 μm.

However, if the size of ferritin clusters is smaller than $\widetilde{R}$ ($R < \widetilde{R}$), the criterion in Eq. (18) is not satisfied and a theory that accounts for the effect of molecular diffusion on signal decay should be applied. Herein we use the GPA approach (Sukstanskii and Yablonskiy 2003; Sukstanskii and Yablonskiy 2004). In (Sukstanskii and Yablonskiy 2004), the theory has been developed for the case of impermeable (for diffusing water molecules) inclusions, whereas in (Sukstanskii and Yablonskiy 2003) – for permeable inclusions.

Qualitatively, in both cases, the TE-dependence of the GRE signal induced by the spherical susceptibility inclusions in the GPA is similar to that in the SDR: the logarithm of the signal is characterized by a quadratic dependence at short TE and a linear one at long TE. The transition between the regimes takes place at the transition time $\sim R^2 / D$, which is different from the transition time $t_* = 1.5 / \delta\omega_f$ in the SDR. For clusters with $R < 0.4$ μm this transition time is shorter than 1 ms, which is smaller than the first gradient echo time in our experiments (see Methods section below). Thus, in our experimental settings, the contribution of the non-heme iron to the signal decay in the motion narrowing regime (MNR) can be characterized by a mono-exponential factor with the relaxation rate constant,

$$R2t^*_{nhi} = \lambda_{MNR} \cdot \Delta\chi_{nhi}. \tag{20}$$

where the proportionality coefficients for the permeable spheres differ from the impermeable case by a numerical factor 0.9:

$$\lambda_{MNR} = \begin{cases} \frac{32}{45} \cdot \gamma B_0 \cdot (\delta\omega_f \cdot t_D), \text{ impermeable} \\ \frac{16}{25} \cdot \gamma B_0 \cdot (\delta\omega_f \cdot t_D), \text{ permeable} \end{cases} \tag{21}$$

where $t_D = R^2 / 6D$ is the characteristic diffusion time.

3. Methods

Data were obtained from 22 healthy control participants (ages 26–63 years, 6 males, 16 female) with the local IRB approval from Washington University in Saint Louis. The written informed consent was obtained from all participants.

The qGRE data were acquired with a 3T Trio MRI scanner (Siemens, Erlangen, Germany) using a three-dimensional (3D) multi-gradient-echo sequence with monopolar readout and slab-selection RF-gradient pulse, FOV 256 × 192 × 144 mm^3, repetition time $TR = 50$ ms, flip angle 30°, 10 gradient echoes with first gradient echo time, $TE_1 = 4$ ms, echo spacing $\Delta TE = 4$ ms, voxel size 1 × 1 × 2 mm^3, acquisition time 13 min. An additional phase stabilization echo (the navigator) was collected for each line in the k-space to correct for image artefacts due to the physiological fluctuations (Wen et al., 2015). After data acquisition, the raw k-space data were read into MATLAB (The MathWorks, Inc.) for post-processing. Then, after correcting the k-space data for physiological fluctuations (Wen et al., 2015), FFT was applied to get images. The multi-channel data were combined on a voxel-by-voxel basis, using the weighting algorithm that provides for the optimal model parameters estimation (Quirk et al., 2009; Luo et al., 2012):

$$\begin{aligned} S_{comb}(TE_n) &= \sum_{m=1}^{M} \eta_m \cdot S_m(TE_n) \cdot \bar{S}_m(TE_1) \\ \eta_m &= \frac{1}{M\sigma_m^2} \cdot \sum_{m'=1}^{M} \sigma_{m'}^2 \cdot \left[\sum_{m'=1}^{M} |\, S_{m'}(TE_1) \,|^2 \right]^{-1/2} \end{aligned} \tag{22}$$

where $S_m(TE_n)$ is the signal measured on the m^{th} channel ($m = 1, 2, \ldots, M$, M is a number of channels) at the n^{th} sampling time TE_n ($n = 1, 2, \ldots, N$, N is a number of gradient echoes in a pulse sequence), $\bar{S}_m$ denotes complex conjugate of S_m, η_m are weighting factors, and σ_m are noise amplitudes. Note also that the algorithm in Eq. (22) automatically removes the initial phase incoherence among the channels (Luo et al., 2012). The noise level in each channel was evaluated by averaging data from small (e.g., 10 × 10 pixels) area in the corner of magnitude images $| S_m(TE_n) |$ and then averaging across 10 gradient echoes.

3D spatial Hanning filter was applied to the data in the image domain to reduce Gibbs ringing artefacts and increase signal-to-noise ratio (SNR) in the analysis of the qGRE data. The multi-gradient echo (complex) qGRE signal was analyzed by fitting the expression in Eq. (1) to experimental data on the voxel-by-voxel basis. The function $F_{macro}(TE)$ accounting for the effects of macroscopic magnetic field inhomogeneities, was calculated using magnitude and phase of the same multi-gradient echo signal and the method developed in (Yablonskiy et al., 2013b). Importantly, this calculation does not bring any additional fitting parameters to the model in Eq. (1). The fitting parameters are the amplitude S_0, the tissue-specific relaxation rate constant $R2t^*$, the BOLD-related parameters $dCBV$ and $\delta\omega_h$, and the frequency shift Δf. Several steps were adopted to mitigate adverse effects of the noise in the data. (i) A two-stage fitting procedure was used for a voxel-by-voxel fitting of theoretical model, Eq. (1), to multi-gradient-echo data. After first fitting step, spheres with the radii of two voxels in the GM and five voxels in the white matter were selected around each voxel for calculating a median value of $\delta\omega_h$, that was subsequently assigned to this voxel's $\delta\omega_h$ value and kept constant during the second round of voxel-by-voxel fitting. This reduces the number of fitting parameters, making fit more stable. The choice of fixing $\delta\omega_h$ (that is proportional to oxygen extraction fraction (Yablonskiy and Haacke 1994) for the second round of fitting is due to the fact that oxygen extraction fraction maps are relatively flat despite significant differences in regional oxygen consumption and blood flow (Powers et al., 1987). The parameters $dCBV$ and $\delta\omega_h$ are subsequently used to calculate $R2'_{BOLD}$ that is used for evaluation of $\Delta\chi_{heme}$ per Eq. (10). (ii) As demonstrated in (Zhao et al., 2016), median values of parameters calculated across large regions of interest reduce the role of noise-related outliers and provide reliable estimate of actual parameters. Hence, only median values of parameters for selected regions are reported in this paper.

The phase of qGRE signal was used to generate QSM maps of the magnetic susceptibility $\Delta\chi_{QSM}$ (Reichenbach et al., 2015; Wang and Liu 2015) with programs available at http://weill.cornell.edu/mri/pages/qsm.html. First, the frequency offset was evaluated using a voxel-wise complex fitting (with the function "Fit_ppm_complex_TE"). Second, the frequency maps were unwrapped using a region-growing algorithm (with the function "unwrapPhase"). Then, background fields were removed using the Projection onto Dipole Fields (PDF) algorithm. Finally, QSM maps were calculated using the Morphology enabled dipole inversion technique with parameter "lambda" equaled 1000.

Note that QSM does not produce absolute values of local magnetic susceptibilities. However, there is no generally adopted region in the brain that could be used as an independent reference. Even CSF in the ventricles shows variation in QSM measurements.

In this paper, we use QSM values averaged across cortical GM as a reference region. Since the concentration of non-heme iron in cortical GM is significantly lower than in the basal ganglia (Hallgren and Sourander 1958a), by subtracting QSM values of the cortical GM from generated QSM maps, we also minimize cellular contribution to our measurements of iron contribution to QSM in basal ganglia (see Eq. (11)). To further account for contribution of heme iron, we also subtract heme iron contribution of cortical GM from QSM values of cortical GM.

Finally, using Eqs. (10-11), the volume magnetic susceptibilities of heme iron $\Delta\chi_{heme}$ and non-heme iron $\Delta\chi_{nhi}$ can be calculated. Our analysis was applied to three regions of basal ganglia with high iron accumulation: caudate, putamen, and pallidum. All brain segmentations were performed using FreeSurfer software (Laboratory for Computational Neuroimaging Martinos Center for Biomedical Imaging (Iglesias et al., 2015)).

The data that support the findings of this study are available from the corresponding author upon reasonable request. All the data analyses were done using programs written in MATLAB (code available upon request from the corresponding author).

4. Results

An example of S_0 (T1-weighted image), $R2^*$, $R2t^*$, $R2'_{BOLD}$ and QSM maps reconstructed from the qGRE signal from a healthy volunteer MRI scans are shown in Fig. 1. The contrast of basal ganglia is clearly visualized in all maps.

Fig. 2 demonstrates the age-dependence of tissue total magnetic susceptibility as well as contributions to tissue magnetic susceptibilities of heme- and non-heme iron in caudate, putamen, and pallidum. Similar linear dependences for the *total susceptibility* were observed in other brain structures, e.g., in dentate nucleus (Li et al., 2014), and substantia nigra (Liu et al., 2016).

Note that the contribution of heme iron in deoxyhemoglobin to the tissue volume magnetic susceptibility only slightly increases with age, whereas the contribution of non-heme iron to the tissue volume magnetic susceptibility shows more pronounced effect (see regression coefficients in Fig. 2), especially in the pallidum. The statistical significance of age effect is shown in Fig. 2.

The regression analysis of $R2t^*$ vs. $\Delta\chi_{nhi}$ of the combined data (three ROIs in each of 22 participants) resulted in the following linear dependence ($R^2 = 0.85$) shown in Fig. 3:

$$R2t^* = R2t_{cell}{}^* + R2t_{nhi}{}^* = 14.6 + 122.5 \cdot \Delta\chi_{nhi}[\text{ppm}] \quad (23)$$

Note that in Eq. (23) and the following numerical Eqs. (24) and (25), the $R2t^*_{nhi}$ is in s^{-1}, and $\Delta\chi_{nhi}$ is in ppm.

While the last term in Eq. (23) shows $R2t^*$ dependence on the tissue magnetic susceptibility of non-heme iron, the first term is associated with the cellular contribution (as in Eq. (2)).

Combining Eqs. (23) and (3), we obtain the NDI in the basal ganglia: $NDI = 0.43$ which is at the lower end of data reported for the cortical GM (Wen et al., 2018).

Results in Eq. (23) can be further compared with the theoretical predictions in Eqs. (16) and (20). Combining the numerical parameters entering Eqs. (16) and (20), the relationships between $R2t^*_{nhi}$ and $\Delta\chi_{nhi}$ in the two approaches at $B_0 = 3\text{T}$ are as follows:

$$R2t^*_{nhi} = \lambda_{SDR} \cdot \Delta\chi_{nhi}\ [\text{ppm}], \qquad \lambda_{SDR} = 324.2\,\text{s}^{-1} \tag{24}$$

in the static dephasing regime and

$$R2t^*_{nhi} = \lambda_{MNR} \cdot \Delta\chi_{nhi}[\text{ppm}], \qquad \lambda_{MNR} = 0.528\,\text{s}^{-1} \tag{25}$$

in the motional narrowing regime for randomly distributed ferritin complexes (*no clustering*).

By comparing the experimentally obtained coefficient $\lambda_{\text{exp}} = 122.5\,\text{s}^{-1}$ / ppm in the last term in Eq. (23) with the theoretical predictions in Eqs. (24) and (25), we can see that neither SDR nor MNR for non-clustered ferritin can explain experimental results. In the SDR, the coefficient $\lambda_{SDR} = 324.2\,\text{s}^{-1}$ / ppm. is almost 3 times bigger that in Eq. (23). According to Eq. (16), λ_{SDR} depends only on the external field B_0, i.e. there is no "adjustable" parameter to explain the discrepancy between λ_{SDR} and λ_{exp}. That is why one can conclude that in our experimental conditions the SDR cannot describe the non-heme iron contribution to the GRE signal decay. The discrepancy between the prediction of the motional narrowing regime with non-clustered ferritin complexes and experimental measurements is even more striking: $\lambda_{MNR} \approx 0.5\,\text{s}^{-1}$ / ppm vs. $\lambda_{\text{exp}} = 122.5\,\text{s}^{-1}$ / ppm. However, Eqs. (20) for λ_{MNR} contain one additional parameter, $t_D = R^2 / 6D$. Therefore, if the ferritin complexes are not randomly distributed but aggregated in the clusters of size R_c with many units, the coefficient λ_{MNR} increases proportionally to R_c^2. It is easy to verify that $\lambda_{MNR} = \lambda_{\text{exp}}$ if the cluster size $R_c = 96$ nm for water-impermeable clusters and $R_c = 101$ nm for a case of water-permeable clusters. An upper limit of a number of individual ferritin complexes in a cluster (N_c) depends on their spatial distribution. For densely packed clusters (a case when an average distance between nearest ferritin complexes is much smaller than the size of the ferritin complex), N_c can be estimated as

$$N_c \approx \eta \cdot \left(\frac{R_c}{R_{ext}}\right)^3, \qquad \eta = \frac{\pi}{3\sqrt{2}} \tag{26}$$

where $\eta \approx 0.74$ is a numerical coefficient. Hence, a densely packed cluster of radius $R_c = 96$ nm can comprise up to $N_c \approx 2650$ individual ferritin shells with radius of $R_{ext} = 6.25$ nm. However, if the clusters are loosely, rather than densely packed, so that an average distance between neighboring ferritin complexes in the clusters is on the order of the ferritin complex's size (see, for example, Fig. 4 in (Quintana et al., 2006)), the number N_c can be estimated by replacing R_{ext} in Eq. (26) with $\bar{R}_{ext}$ - a half the average distance between nearest ferritin complexes.

Importantly, the predicted radius of the clusters ($R_c \approx 100$) is well below the upper limit of the GPA's validity (Eq. (18)), $R_c < \tilde{R} = 400$ nm. Besides, although the transition time between the quadratic and linear regimes corresponding to such a cluster ($\sim R_c^2 / 6D \approx 1$ μs) is substantially longer than for a single ferritin shell, it still remains much shorter than the first gradient echo time in our experiments ($TE_1 = 4$ ms). Consequently, the non-heme iron contribution to the signal decay can be described in the motion narrowing regime by the relaxation rate constant $R2t^*_{nhi}$:

$$R2t^*_{nhi} = \lambda' \cdot \Delta\chi_{nhi}$$
$$\lambda' = \begin{cases} \frac{32}{45} \cdot \gamma B_0 \cdot \left(\delta\omega_f \cdot R_c^2 / 6D\right), \ densely-packed \quad clusters \\ \frac{16}{25} \cdot \gamma B_0 \cdot \left(\delta\omega_f \cdot R_c^2 / 6D\right), \ loosely-packed \quad clusters \end{cases} \tag{27}$$

In Eq. (27) we use the definition of diffusion time t_D from Eq. (21) with the radius corresponding to the ferritin cluster R_c. Note that in Eq. (27) the impermeable result from Eq. (21) (first line) is used for densely-packed clusters and the permeable result (second line) is used for loosely-packed clusters (in this case water molecules can diffuse within the clusters between ferritin complexes).

Combining Eqs. (12), (15) and (27), the coefficient λ' can be presented as

$$\lambda' = \begin{cases} \frac{4}{135\pi} \cdot (\gamma B_0)^2 \cdot \frac{N_i \cdot R_c^2}{R_{ext}^3 \cdot D} \cdot \left(\frac{\mu_0 \mu_{eff}^2}{3k_B T}\right), \ densely-packed \ clusters \\ \frac{2}{75\pi} \cdot (\gamma B_0)^2 \cdot \frac{N_i \cdot R_c^2}{\bar{R}_{ext}^3 \cdot D} \cdot \left(\frac{\mu_0 \mu_{eff}^2}{3k_B T}\right), \quad loosely-packed \ clusters \end{cases} \tag{28}$$

Here again, $R_{ext} = 6.25$ nm for densely packed clusters and $\bar{R}_{ext}$ is a half the average distance between nearest ferritin complexes for loosely-packed clusters.

5. Discussion

Our study aims at quantitative in vivo evaluation of heme iron, non-heme iron, and tissue cellular content in three iron-rich regions of basal ganglia - putamen, caudate, and pallidum. Magnitude and phase images are used to reconstruct the qGRE metrics ($R2^*$, $R2t^*$, $R2'_{BOLD}$), which are generated by a multi-gradient echo sequence. The QSM maps reconstructed from the phase images (Reichenbach et al., 2015; Wang and Liu 2015) provide information on tissue magnetic susceptibility that includes contribution from all tissue components, i.e. cells, heme iron in blood vessels, non-heme iron, etc. The combination of magnitude and phase images is analyzed using qGRE approach (Ulrich and Yablonskiy 2016) and theoretical models that account for GRE signal decay due to the presence of cells (Wen et al., 2018), iron in blood vessels (BOLD effect), non-heme iron, and macroscopic field inhomogeneities (background B_0 field gradients).

The BOLD component factor is analyzed in the framework of the static dephasing regime (Yablonskiy and Haacke 1994), whereas the ferritin contribution required accounting for water molecule diffusion around ferritin complexes; the Gaussian Phase Approximation (GPA) (Sukstanskii and Yablonskiy 2003; Sukstanskii and Yablonskiy 2004) was used to account for this effect. The combination of QSM and qGRE approaches allowed us to disentangle contribution of all these tissue components to the qGRE signal as well as the contribution of unwanted macroscopic magnetic field inhomogeneities (Yablonskiy et al., 2013). Importantly, our pulse sequence design and post-processing approach made it possible to analyze all these contributions from a single measurement.

The difference in describing contributions of heme iron (BOLD effect) and non-heme iron to the GRE signal decay stems from the different sizes of heme-iron-containing blood vessels and the ferritin complexes. The SDR is valid for sufficiently large magnetic susceptibility inclusions when the GRE signal dephasing is not affected by the molecular diffusion (Yablonskiy and Haacke 1994). Theoretical discussion of SDR applicability to BOLD effect was provided in (Yablonskiy and Haacke 1994), followed by a validation on phantoms (Yablonskiy 1998) and animal studies (He et al., 2008). Radii of blood vessels are several micrometers and higher, therefore the SDR can adequately describe the BOLD-related signal decay (Dickson et al., 2011). However, for ferritin iron, water diffusion might play an important role and the SDR can be used only if the ferritin complexes are aggregated in cluster with radius $R > \tilde{R}$ (Eq. (18)). Comparison of the predictions of these two models with the experimental measurements, demonstrated that the SDR would significantly overestimate contribution of non-heme iron to GRE signal decay, while the GPA theory can adequately describe experimental data assuming that the ferritin complexes are aggregated in clusters with the radius $R_c = 96$ nm (up to 2650 individual ferritin shells).

The fact that the SDR would significantly overestimate contribution of iron measured by QSM to the GRE signal decay was also pointed out in (Taege et al., 2019), however, their treatment of the phenomenon did not include separation of heme and non-heme iron contributions and was based on a synthetic equation combining effects of static dephasing and motional narrowing regimes.

Our estimates of the cluster size R_c are in a qualitative agreement with the results seen in studies of ferritin and/or hemosiderin in human brain (Connor et al., 1990) (Quintana et al., 2006), and liver (Ghugre et al., 2005), that clearly demonstrated clustering with the aggregate sizes in the range of hundreds nm. It should be noted however, that the cluster size $R_c = 96$ was estimated under assumption that the iron loading factor is equal to its maximal value ($N_i = 4500$) and the diffusion coefficient is assumed to be equal to $D = 1\mu m^2 / ms$. However, the diffusion coefficient varies across brain regions and also can change with disease, the loading factor can also be different from its maximum value (ten Kate, Wolthuis et al. 1997). To account for these variations (if they are measured independently), for a given coefficient λ' in Eq. (28), the cluster size should be scaled as $R_c \sim (D / N_i)^{1/2}$. Hence, a lower value of N_i and/or a higher value of D would result in a bigger cluster size R_c. For instance, $N_i = 2250$ (50% of its maximal value) and $D = 2\mu m^2 / ms$ would correspond to $R_c = 192$nm.

The regression analysis of experimental measurements on 22 healthy participants in putamen, caudate, and pallidum revealed that the parameters $R2t^*$ and $\Delta\chi_{nhi}$ are linearly related, Eq. (23). The $\Delta\chi_{nhi}$-independent term in Eq. (23) can be associated with the cellular contribution to the relaxation rate constant ($R2t^*_{cell}$), which is mostly related to the neuronal density in GM (Wen et al., 2018).

Non-heme iron susceptibility $\Delta\chi_{nhi}$ can be related to non-heme iron concentration [Fe]:

$$\Delta\chi_{nhi} = \nu \cdot [Fe], \quad \nu = \left(\frac{\mu_0\mu^2_{eff}}{3k_BT}\right) \cdot \frac{N_a \cdot \rho_t}{M_{Fe}}. \tag{29}$$

At $T = 301^{\circ} K$, it gives $\nu = 1.3$ ppb/(μg Fe/g) that is in a rather good agreement with experimentally found value ~ 1 ppb/(μg Fe/g) (Liu et al., 2016).

Using Eqs. (20) and (27), a similar relationship can be established for the relaxation rate constant $R2t^*_{nhi}$:

$$R2t^*_{nhi} = \eta \cdot [Fe], \quad \eta = \lambda' \cdot \nu \tag{30}$$

where the coefficient λ' is given in Eq. (28). In contrast to the coefficient ν in Eq. (29), the coefficient η depends not only on the characteristics of non-heme iron, but also on the specific iron distribution: loading factor N_l (number of iron molecules inside the ferritin shell), the average distance between ferritin units and the radius of ferritin cluster R_c. That is why a value of this coefficient is not universal and can vary across the brain. For $N_l = 4500$ and $R_c = 96$ nm, we find $\lambda' = 122.5 \cdot 10^6 s^{-1}$ (at 3T), and $\eta = 0.17$. This value is in a range of reported literature values (0.11 – 0.27) of the coefficients relating the relaxation rate constant $R2^*$ and iron concentration obtained at $B_0 = 3$ T Peran et al., 2009; Yao et al., 2009; Langkammer et al., 2010; Langkammer et al., 2012; Li et al., 2014; Sedlacik et al., 2014; Barbosa et al., 2015)). It should be noted, however, that in previous studies (Peran et al., 2009; Yao et al., 2009; Langkammer et al., 2010; Langkammer et al., 2012; Li et al., 2014; Sedlacik et al., 2014; Barbosa et al., 2015) heme and non-heme iron contributions were not separated and the regression coefficient provided an association between the total iron concentration and the total GRE signal relaxation rate $R2^*$, whereas the parameter η in our approach (Eq. (30)) relates only the non-heme iron concentration $\Delta\chi_{nhi}$ to $R2t^*_{nhi}$ - the non-heme iron specific part of $R2^*$. In the regions of very high iron accumulation (e.g. pallidum), the fraction of heme iron is relatively small and its contribution to $R2^*$ is small as compared with the non-heme iron. However, in regions like caudate and putamen, the magnetic susceptibility of heme iron is about 25% of the total iron magnetic susceptibility (Fig. 2). Given that the relaxivity of heme iron is about two times higher than the relaxivity of non-heme iron (compare Eqs. (10) and ((23)), the $R2^*$-based error in estimation of non-heme iron magnetic susceptibility can be about 70%. This error can be significantly higher in regions with even lower concentration of non-heme iron, e.g. in the cerebral cortex.

It is important to emphasize that our theory predicts a quadratic dependence of the relaxation rate constant $R2t^*_{nhi}$ on the external field B_0 Eqs. (28), ((30)). Hence, the B_0-dependence of the *total* transverse relaxation rate constant $R2^* = R2t^* + R2'_{BOLD} = R2t^*_{nhi} + R2t^*_{cell} + R2'_{BOLD}$ can vary from linear (when the BOLD-related term $R2'_{BOLD} \sim B_0$ dominates) to quadratic (when $R2t^*_{nhi} \sim B_0^2$ plays the major role).

It should also be noted that our calculations of ferritin magnetic susceptibility were based on the experiments (Michaelis et al., 1943; Quintana et al., 2004) suggesting that the ferritin obeys the Curie law with an effective magnetic moment $\mu_{eff} = 3.8\,\mu_B$. However, several studies of ferritin in the broad range of the external magnetic fields and temperatures (e.g., (Brooks et al., 1998; Gilles et al., 2002; Ropele and Langkammer 2017) and references therein) suggest that the actual magnetic structure of the ferritin iron is more complicated. According to (Brooks et al., 1998), the central core is antiferromagnetic. However, the incomplete cancelation of antiparallel moments may result in the existence of the superparamagnetic moment. In more recent analysis (Quintana et al., 2004; Resnik 2004), it was suggested the presence of more than one crystalline antiferromagnetic or ferrimagnetic phases (i.e. hematite Fe_2O_3, magnetite Fe_3O_4, maghemite γ-Fe_2O_3), which contribute to the superparamagnetic properties of the interior core (Quintana et al., 2004; Resnik 2004). The different phases may have different magnetic moments μ_{eff}. The detail description of the current view on this problem can be found in the recent review paper (Ropele and Langkammer 2017). However, more experimental data on the ferritin structure would be required for developing more detail theoretical model.

As these fine details of ferritin structure are not clear yet, the values of the ferritin magnetic susceptibility $\Delta\chi_{nhi}$ and the characteristic frequency $\delta\omega_f$ can be different from those calculated on the basis of Curie's Law as in Eq. (12) with an "effective magnetic moment" μ_{eff}. However, as noted in (Brooks et al., 1998), this description is rather "coincidental", hence should be used with caution. Nevertheless, regardless of the specific values μ_{eff} (and, consequently, of $\Delta\chi_{nhi}$ and $\delta\omega_f$), our analysis demonstrates that the non-heme iron contribution to the relaxation rate constant $R2t^*$ can be described in the motion narrowing regime, provided that the ferritin complexes are aggregated in clusters. Moreover, Eq. (27) demonstrates that if a new experimental evidence will arise requiring changes in the ferritin magnetic susceptibility, a sole parameter that should be adjusted in Eq. (27) to describe experimental data is the clusters' size. Fig. 4 illustrates the dependence of the cluster radius R_c on the frequency $\delta\omega_f$ ($R_c \sim \delta\omega_f^{-1/2}$) that is directly related to the ferritin magnetic susceptibility, $\Delta\chi_{nhi}$ per Eq. (15).

In this paper we use quantitative relationships, Eq. (3), established in (Wen et al., 2018) between cortical GM cellular composition and the $R2t^*$ metric of the quantitative Gradient Recalled Echo (qGRE) MRI signal. This relationship allows estimation of the $R2t^*$ -defined neuronal density index (NDI) in the cortical GM – a parameter proportional to the density of neurons. It is important to note that neuron in this approach is considered as a structure comprised of cell body and neuronal processes - axons and dendrites. While details of the cellular composition in the deep GM are different from the cortical GM, the relationship in

Eq. (3) can still provide information on NDI because it was demonstrated in (Wen et al., 2018) that neurons are about five times stronger endogenous contrast agent than the glia cells.

Our approach is based on the methods that rely on biophysical model of GRE signal formation in deep GM that accounts for water signal relaxation due to the presence of cells as well as heme and non-heme iron. The framework for this approach is discussed in detail in the Theory and Discussion sections. Two other potentially confounding factors should also be discussed. First, the mono-exponential TE-dependence of the tissue-related factor in Eq. (1) (described by the relaxation rate constant $R2t^*$) is, obviously, an approximation. More complicated models, accounting for multi-compartment structure of the brain could include a multi-exponential description. Such a behavior was previously proposed and observed in white matter mostly due to a presence of water trapped between myelin layers (Wharton and Bowtell 2012; Sati et al., 2013; Sukstanskii and Yablonskiy 2014). In fact, such a behavior was also observed in our data in white matter (data not shown) but no evidence for a multi-component behavior was seen in our data in GM. While experiments with higher SNR and longer gradient echo times could potentially provide more detailed information on GM multi-component structure, an analysis of such models is beyond the scope of the present study. We should also note that multi-component models at short echo times could also mimic a quadratic TE-dependence of the GRE signal in a log scale, as in our BOLD mode. However, this quadratic behavior would have a different curvature sign – concave for multi-component signal vs. convex for the BOLD effect. Our data in GM always show convex pattern for short gradient echo times TE suggesting the presence of the BOLD effect (see detail discussion in (Ulrich, 2016) and no evidence for a multi-component behavior. Second, for quantifying non-heme iron, we used Eq. (11) that included the term $\Delta\chi_{cell}$ that was accounted for in our approach by referencing QSM measurements to the QSM values of cortical GM adjusted for the presence of heme iron. However, since cortical GM also contains non-heme iron, our results actually provide not absolute values, but the difference between non-heme iron concentration in selected regions of basal ganglia and averaged values in cortical GM. Since concentration of non-heme iron in Globus pallidum is 4 to 10 times higher than in the cortical regions (Hallgren and Sourander 1958b), our measurements in Globus pallidum are quite accurate. However, in Putamen and Caudate nucleus concentration of non-heme iron is only 2 to 4 times higher than in the cortical regions (Hallgren and Sourander 1958a), hence leading to 20–30% underestimation of actual non-heme iron content.

Conclusion

Quantitative Gradient Recalled Echo (qGRE) MRI technique based on the GRE sequence with multiple gradient echoes and theoretical model of GRE signal formation allows separation of the total $R2^*$ metric characterizing decay of GRE signal into tissue specific ($R2t^*$) and baseline BOLD ($R2'_{BOLD}$) contributions. A combination with the QSM data (also available from phase information of the qGRE signal), allowed further separation of the tissue-specific $R2t^*$ metric in a tissue-cellular specific and non-heme-iron-specific contributions in iron-rich basal ganglia.

It was shown that the non-heme iron contribution can be described in the motion narrowing regime with the ferritin complexes aggregated in clusters with an average radius $R_c \approx 100$ nmcomprising up to 2650 individual ferritin units. It was also demonstrated that tissue concentrations of heme and non-heme iron tend to increase with age. The strongest age effect was seen in the pallidum where the highest age-related non-heme iron accumulation was observed.

Acknowledgment

This work was supported by NIH R01AG054513 and grant 20140257 from the Marilyn Hilton Award for Innovation in MS Research.

References

Barber TW, Brockway JA, Higgins LS, 1970. The density of tissues in and about the head. Acta Neurol. Scand 46 (1), 85–92. [PubMed: 4983875]

Barbosa JH, Santos AC, Tumas V, Liu M, Zheng W, Haacke EM, Salmon CE, 2015. Quantifying brain iron deposition in patients with Parkinson's disease using quantitative susceptibility mapping, R2 and R2. Magn. Reson. Imaging 33 (5), 559–565. [PubMed: 25721997]

Brooks RA, Vymazal J, Goldfarb RB, Bulte JW, Aisen P, 1998. Relaxometry and magnetometry of ferritin. Magn. Reson. Med 40 (2), 227–235. [PubMed: 9702704]

Connor JR, Menzies SL, Martin SMS and Mufson EJ (1990). "Cellular distribution of transferrin, ferritin, and iron in normal and aged human brains." 27(4): 595–611.

Cornell RM, Schwertmann U, 2003. The Iron Oxides: Structure, Properties, Reactions, Occurrences, and Uses. Wiley-VCH Verlag GmbH, Weinheim.

Dickson JD, Ash TW, Williams GB, Sukstanskii AL, Ansorge RE, Yablonskiy DA, 2011. Quantitative phenomenological model of the BOLD contrast mechanism. J. Magn. Reson 212 (1), 17–25. [PubMed: 21782488]

Ghugre NR, Coates TD, Nelson MD, Wood JC, 2005. Mechanisms of tissue-iron relaxivity: nuclear magnetic resonance studies of human liver biopsy specimens. Magn. Reson. Med 54 (5), 1185–1193. [PubMed: 16215963]

Gilles C, Bonville P, Rakoto H, Broto JM, Wong KKW, Mann S, 2002. Magnetic hysteresis and superantiferromagnetism in ferritin nanoparticles. J. Magn. Magn. Material 241, 430–440.

Hallgren B, Sourander P, 1958a. The effect of age on the non-haemin iron in the human brain. J. Neurochem 3 (1), 41–51. [PubMed: 13611557]

Hallgren B, Sourander P, 1958b. The effect of age on the non-haemin iron in the human brain. J. Neurochem 3 (1), 41–51. [PubMed: 13611557]

He X, Zhu M, Yablonskiy DA, 2008. Validation of oxygen extraction fraction measurement by qBOLD technique. Magn. Reson. Med 60 (4), 882–888. [PubMed: 18816808]

Iglesias JE, Augustinack JC, Nguyen K, Player CM, Player A, Wright M, Roy N, Frosch MP, McKee AC, Wald LL, Fischl B, Van Leemput K, Alzheimer's Disease Neuroimaging, I., 2015. A computational atlas of the hippocampal formation using ex vivo, ultra-high resolution MRI: application to adaptive segmentation of in vivo MRI. Neuroimage 115, 117–137 . [PubMed: 25936807]

Krebs N, Langkammer C, Goessler W, Ropele S, Fazekas F, Yen K, Scheurer E, 2014. Assessment of trace elements in human brain using inductively coupled plasma mass spectrometry. J. Trace Elem. Med. Biol 28 (1), 1–7. [PubMed: 24188895]

Langkammer C, Krebs N, Goessler W, Scheurer E, Ebner F, Yen K, Fazekas F, Ropele S, 2010. Quantitative MR imaging of brain iron: a postmortem validation study. Radiology 257 (2), 455–462. [PubMed: 20843991]

Langkammer C, Schweser F, Krebs N, Deistung A, Goessler W, Scheurer E, Sommer K, Reishofer G, Yen K, Fazekas F, Ropele S, Reichenbach JR, 2012. Quantitative susceptibility mapping (QSM) as

a means to measure brain iron? A post mortem validation study. Neuroimage 62 (3), 1593–1599. [PubMed: 22634862]

Li W, Wu B, Batrachenko A, Bancroft-Wu V, Morey RA, Shashi V, Langkammer C, De Bellis MD, Ropele S, Song AW, Liu C, 2014. Differential developmental trajectories of magnetic susceptibility in human brain gray and white matter over the lifespan. Hum. Brain Mapp 35 (6), 2698–2713. [PubMed: 24038837]

Liu M, Liu S, Ghassaban K, Zheng W, Dicicco D, Miao Y, Habib C, Jazmati T, Haacke EM, 2016. Assessing global and regional iron content in deep Gray Matter as a function of age using susceptibility mapping. J. Magn. Reson. Imaging 44 (1), 59–71. [PubMed: 26695834]

Luo J, Jagadeesan BD, Cross AH, Yablonskiy DA, 2012. Gradient echo plural contrast imaging–signal model and derived contrasts: T2*, T1, phase, SWI, T1f, FST2* and T2*-SWI. Neuroimage 60 (2), 1073–1082. [PubMed: 22305993]

Michaelis L, Coryell CD, S. G, 1943. The magnetic properties of ferritin and some other colloidal ferric compounds. I. Bid. Chem 148, 463.

Peran P, Cherubini A, Luccichenti G, Hagberg G, Demonet JF, Rascol O, Celsis P, Caltagirone C, Spalletta G, Sabatini U, 2009. Volume and iron content in basal ganglia and thalamus. Hum. Brain Mapp 30 (8), 2667–2675. [PubMed: 19172651]

Powers WJ, Press GA, Grubb RL Jr., Gado M, Raichle ME, 1987. The effect of hemodynamically significant carotid artery disease on the hemodynamic status of the cerebral circulation. Ann. Intern. Med 106 (1), 27–34. [PubMed: 3491558]

Quintana C, Bellefqih S, Laval JY, Guerquin-Kern JL, Wu TD, Avila J, Ferrer I, Arranz R, Patino C, 2006. Study of the localization of iron, ferritin, and hemosiderin in Alzheimer's disease hippocampus by analytical microscopy at the subcellular level. J. Struct. Biol 153 (1), 42–54. [PubMed: 16364657]

Quintana C, Cowley JM, Marhic C, 2004. Electron nanodiffraction and high-resolution electron microscopy studies of the structure and composition of physiological and pathological ferritin. J. Struct. Biol 147 (2), 166–178. [PubMed: 15193645]

Quirk JD, Sukstanskii AL, Bretthorst GL, Yablonskiy DA, 2009. Optimal decay rate constant estimates from phased array data utilizing joint Bayesian analysis. J. Magn. Reson 198 (1), 49–56. [PubMed: 19181549]

Reichenbach JR, Schweser F, Serres B, Deistung A, 2015. Quantitative Susceptibility Mapping: concepts and Applications. Clin. Neuroradiol 25 (Suppl 2), 225–230.

Resnik D, 2004. Modeling of the magnetic behavior of γ-Fe2O3 nanoparticles mineralized in ferritin. J. Appl. Phys 95, 7127.

Ropele S, Langkammer C, 2017. Iron quantification with susceptibility. NMR Biomed. 30 (4).

Sati P, van Gelderen P, Silva AC, Reich DS, Merkle H, de Zwart JA, Duyn JH, 2013. Micro-compartment specific T2* relaxation in the brain. Neuroimage 77 (0), 268–278. [PubMed: 23528924]

Schenck JF, 1992. Health and physiological effects of human exposure to whole-body four-tesla magnetic field during MRI. Ann. NY Acad. Sci 649, 285–301. [PubMed: 1580500]

Schenck JF, Zimmerman EA, 2004. High-field magnetic resonance imaging of brain iron: birth of a biomarker? NMR Biomed. 17 (7), 433–445. [PubMed: 15523705]

Sedlacik J, Boelmans K, Lobel U, Holst B, Siemonsen S, Fiehler J, 2014. Reversible, irreversible and effective transverse relaxation rates in normal aging brain at 3T. Neuroimage 84, 1032–1041. [PubMed: 24004692]

Spees WM, Yablonskiy DA, Oswood MC, Ackerman JJH, 2001. MR Properties of Human Blood at 1.5 Tesla. T1, T2, T2* and Gaussian Relaxation Behavior. Magn. Reson. Med 45, 533–542. [PubMed: 11283978]

Stankiewicz J, Panter SS, Neema M, Arora A, Batt CE, Bakshi R, 2007. Iron in chronic brain disorders: imaging and neurotherapeutic implications. Neurother.: J. Am. Soc. Exp. Neurother 4 (3), 371–386.

Sukstanskii AL, Yablonskiy DA, 2003. Gaussian approximation in the theory of MR signal formation in the presence of structure-specific magnetic field inhomogeneities. J. Magn. Reson 163 (2), 236–247. [PubMed: 12914839]

Sukstanskii AL, Yablonskiy DA, 2004. Gaussian approximation in the theory of MR signal formation in the presence of structure-specific magnetic field inhomogeneities. Effects of impermeable susceptibility inclusions. J. Magn. Reson 167 (1), 56–67. [PubMed: 14987599]

Sukstanskii AL, Yablonskiy DA, 2014. On the role of neuronal magnetic susceptibility and structure symmetry on gradient echo MR signal formation. Magn. Reson. Med 71 (1), 345–353. [PubMed: 23382087]

Taege Y, Hagemeier J, Bergsland N, Dwyer MG, Weinstock-Guttman B, Zivadinov R, Schweser F, 2019. Assessment of mesoscopic properties of deep gray matter iron through a model-based simultaneous analysis of magnetic susceptibility and R2* - A pilot study in patients with multiple sclerosis and normal controls. Neuroimage 186, 308–320. [PubMed: 30445148]

ten Kate J, Wolthuis A, Westerhuis B, van Deursen C, 1997. The iron content of serum ferritin: physiological importance and diagnostic value. Eur. J. Clin. Chem. Clin. Biochem 35 (1), 53–56. [PubMed: 9156568]

Ulrich X, Yablonskiy DA, 2016. Separation of cellular and BOLD contributions to T2* signal relaxation. Magn. Reson. Med 75 (2), 606–615. [PubMed: 25754288]

Wang Y, Liu T, 2015. Quantitative susceptibility mapping (QSM): decoding MRI data for a tissue magnetic biomarker. Magn. Reson. Med 73 (1), 82–101. [PubMed: 25044035]

Wen J, Cross AH, Yablonskiy DA, 2015. On the role of physiological fluctuations in quantitative gradient echo MRI: implications for GEPCI, QSM, and SWI. Magn. Reson. Med 73 (1), 195–203. [PubMed: 24482009]

Wen J, Goyal MS, Astafiev SV, Raichle ME, Yablonskiy DA, 2018. Genetically defined cellular correlates of the baseline brain MRI signal. Proc. Natl. Acad. Sci. U.S.A 115 (41), E9727–E9736. [PubMed: 30254176]

Wharton S, Bowtell R, 2012. Fiber orientation-dependent white matter contrast in gradient echo MRI. Proc. Natl. Acad. Sci. U.S.A 109 (45), 18559–18564. [PubMed: 23091011]

Yablonskiy DA, 1998. Quantitation of intrinsic magnetic susceptibility-related effects in a tissue matrix. Phantom study. Magn. Reson. Med 39 (3), 417–428. [PubMed: 9498598]

Yablonskiy DA, Haacke EM, 1994. Theory of NMR signal behavior in magnetically inhomogeneous tissues: the static dephasing regime. Magn. Reson. Med 32 (6), 749–763. [PubMed: 7869897]

Yablonskiy DA, Sukstanskii AL, He X, 2013a. Blood oxygenation level-dependent (BOLD)-based techniques for the quantification of brain hemodynamic and metabolic properties - theoretical models and experimental approaches. NMR Biomed. 26 (8), 963–986. [PubMed: 22927123]

Yablonskiy DA, Sukstanskii AL, Luo J, Wang X, 2013b. Voxel spread function method for correction of magnetic field inhomogeneity effects in quantitative gradient-echo-based MRI. Magn. Reson. Med 70 (5), 1283–1292. [PubMed: 23233445]

Yao B, Li TQ, Gelderen P, Shmueli K, de Zwart JA, Duyn JH, 2009. Susceptibility contrast in high field MRI of human brain as a function of tissue iron content. Neuroimage 44 (4), 1259–1266. [PubMed: 19027861]

Zhao Y, Wen J, Cross AH, Yablonskiy DA, 2016. On the relationship between cellular and hemodynamic properties of the human brain cortex throughout adult lifespan. Neuroimage 133, 417–429. [PubMed: 26997360]

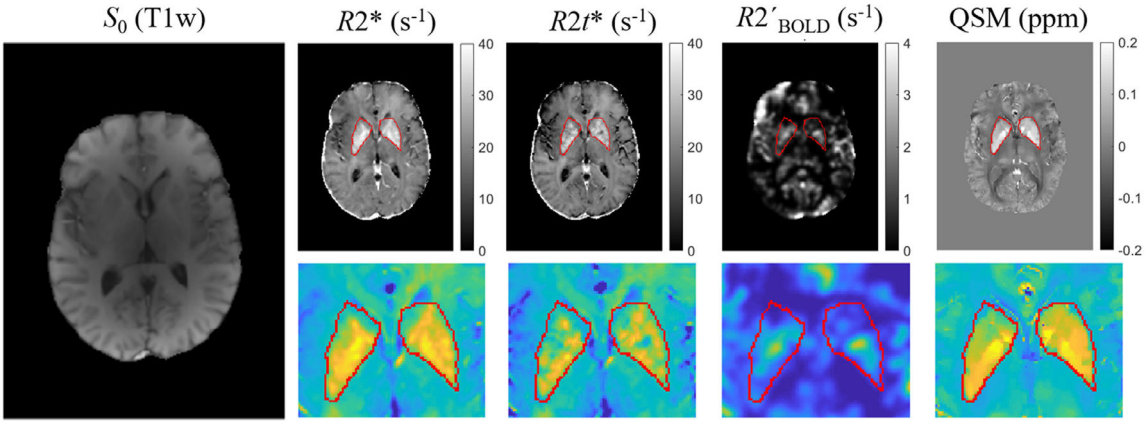

Fig. 1.

An example of images reconstructed from a single MRI acquisition of qGRE signal: S_0 ($T1$-weighted image), the quantitative $R2^*$, $R2t^*$ and $R2'_{BOLD}$ maps, and QSM map (total magnetic susceptibility). The color maps show corresponding enlarged images of the basal ganglia. Data are from a 58-year-old female. Note that in most parts of the brain Gray Matter, including basal ganglia, the values in $R2^*$ maps are higher than in $R2t^*$ maps due to the contribution of the baseline BOLD effect ($R2'_{BOLD}$) to the $R2^*$ maps. However, the differences are relatively small because $R2'_{BOLD} \ll R2t^*$. Also note that not only $R2^*$ and QSM values are increased in the basal ganglia but also $R2t^*$ is increased reflecting the presence of non-heme iron.

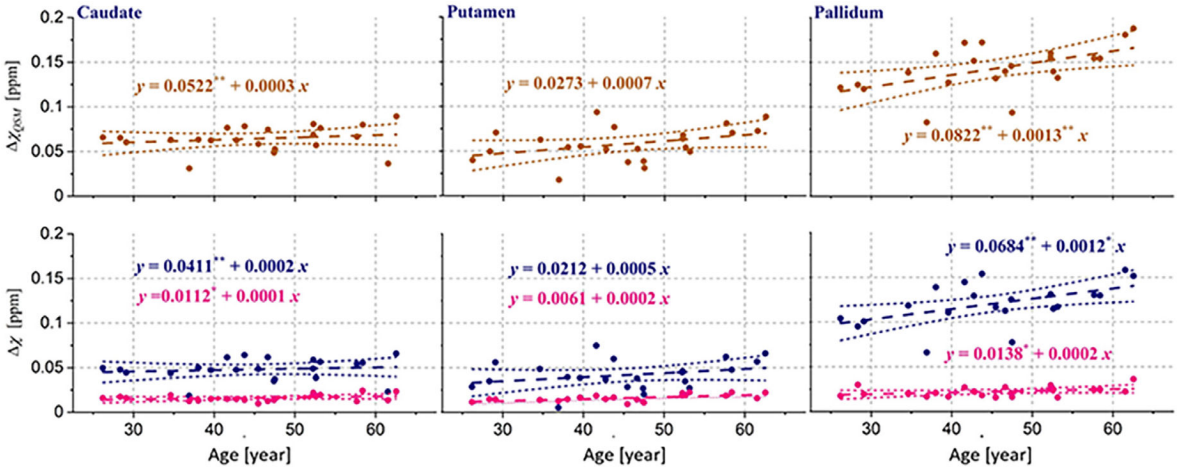

Fig. 2.

The age dependences of the total tissue volume magnetic susceptibility $\Delta\chi_{QSM}$ (brown symbols) and contributions of heme iron in deoxyhemoglobin $\Delta\chi_{heme}$(pink symbols) and non-heme iron $\Delta\chi_{nhi}$ (blue symbols) to tissue volume magnetic susceptibility in caudate, putamen, and pallidum regions. Data obtained from 22 healthy control participants (ages 26–63 years). Each point represents data from a single participant averaged across corresponding region. The linear regression lines and regression coefficients are shown with the corresponding colors. Dotted lines – 95% confidence intervals. Statistical significance of regression coefficients is identified by stars: * corresponds to $P < 0.05$, ** corresponds to $P < 0.01$.

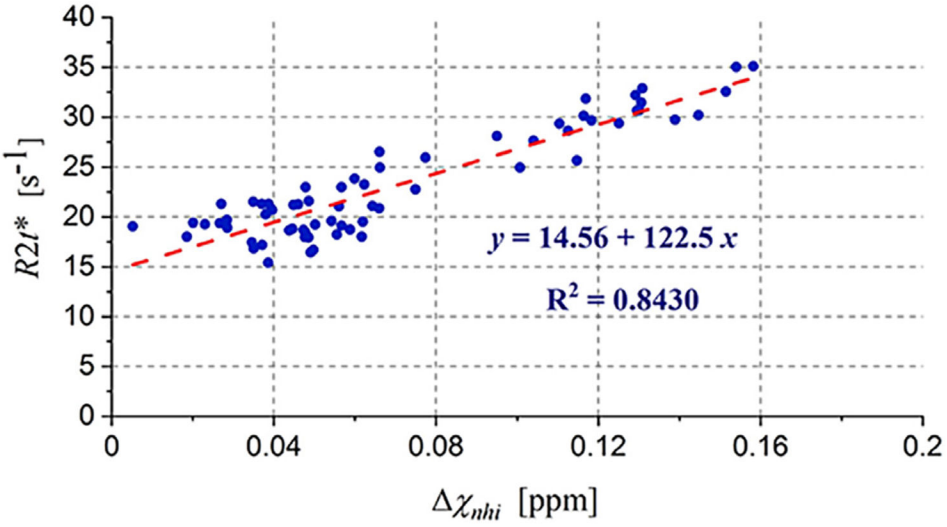

Fig. 3.

The regression analysis of $R2t$ * vs. Δx_{nhi} of the combined data: three ROIs (caudate, putamen, and pallidum) in each of 22 participants. The dashed line corresponds to the linear fit. Each point represents data from a single participant, averaged across the corresponding region. *P*-values for both regression coefficients are smaller than 0.0001.

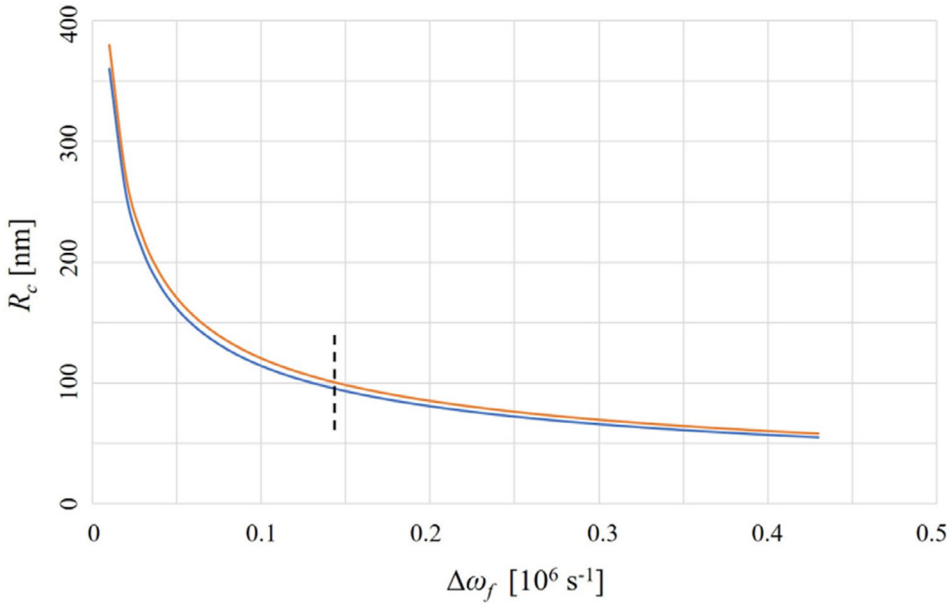

Fig. 4.

The relationship between the cluster radius R_c and the characteristic frequency $\delta\omega_f$ that should be satisfied in order to describe experimental contribution of ferritin to the GRE signal decay. The dash vertical line marks the value of $\delta\omega_f = 0.14 \cdot 10^6\,\mathrm{s}^{-1}$ (corresponding to the currently used ferritin magnetic susceptibility of 529 ppm in Eq. (14)), at which $R_c = 96$ nm for densely-packed (lower curve) and $R_c = 101$ nm for loosely-packed (upper curve) ferritin complexes.